

Fabrication and characterization of thermally actuated micromechanical resonators for airborne particle mass sensing: II. Device fabrication and characterization

This article has been downloaded from IOPscience. Please scroll down to see the full text article.

2010 J. Micromech. Microeng. 20 125019

(<http://iopscience.iop.org/0960-1317/20/12/125019>)

View [the table of contents for this issue](#), or go to the [journal homepage](#) for more

Download details:

IP Address: 130.253.46.131

The article was downloaded on 01/12/2010 at 07:07

Please note that [terms and conditions apply](#).

Fabrication and characterization of thermally actuated micromechanical resonators for airborne particle mass sensing: II. Device fabrication and characterization

Arash Hajjam¹, James C Wilson², Amir Rahafrooz¹ and Siavash Pourkamali¹

¹ Department of Electrical and Computer Engineering, University of Denver, Denver, CO 80208, USA

² Department of Materials and Mechanical Engineering, University of Denver, Denver, CO, 80208, USA

E-mail: spourkam@du.edu

Received 7 May 2010, in final form 18 October 2010

Published 18 November 2010

Online at stacks.iop.org/JMM/20/125019

Abstract

This paper, the second of two parts, presents extensive measurement and characterization results on fabricated thermally actuated single-crystal silicon MEMS resonators analyzed in part I. The resonators have been fabricated using a single mask process on SOI substrates. Resonant frequencies in a few hundreds of kHz to a few MHz and equivalent motional conductances as high as 102 mA V^{-1} have been measured for the fabricated resonators. The measurement results have been compared to the resonator characteristics predicted by the model developed in part I showing a good agreement between the two. Despite the relatively low frequencies, high quality factors (Q) of the order of a few thousand have been measured for the resonators under atmospheric pressure. The mass sensitivities of some of the resonators were characterized by embedding them in a custom-made test setup and deposition of artificially generated aerosol particles with known size and composition. The resulting measured mass sensitivities are of the order of tens to hundreds of Hz ng^{-1} and are in agreement with the expected values based on the resonator's physical dimensions. Finally, measurement of mass density of arbitrary airborne particles in the surrounding lab environment has been demonstrated.

(Some figures in this article are in color only in the electronic version)

1. Introduction

Sensors capable of measuring concentration and size distribution of airborne particles with diameters ranging from a few nanometers to microns have a wide variety of applications. Examples of such applications include urban air quality monitoring, environmental and atmospheric research, and controlled environment monitoring. Scientific research has shown that there is a direct relationship between human life expectancy and the concentration of airborne micro/nanoparticles in the environment [1]. In

atmospheric research, aerosol particles play an important role in the radiation balance of the earth (climate change) [2], and stratospheric ozone depletion [3]. Monitoring particle count in highly controlled environments (e.g. industrial or micro/nanotechnology research cleanrooms) is another important application for such sensors.

Commonly used existing versions of such sensors are either based on optical measurement techniques such as nephelometry [4] and polychromatic LED techniques [5], scanning electron microscopy (SEM) [6], or conventional resonant mass sensors such as surface acoustic wave (SAW)

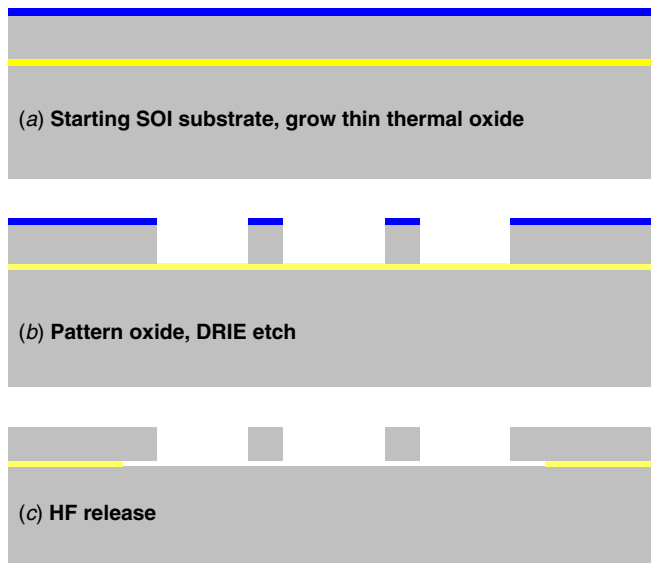


Figure 1. Schematic cross-sectional view of the process flow used for fabrication of the resonators on SOI substrates.

resonators [7, 8] resulting in sophisticated, immense and costly instruments that in some cases do not provide the desired sensitivity level [7, 9]. MEMS/NEMS resonators [10–19], as low-cost highly integrated and ultra-sensitive mass sensors, can potentially provide new opportunities and unprecedented capabilities in this area. Such devices can provide orders of magnitude higher mass sensitivity and resolution compared to FBAR [10] or the conventional quartz [20–22] and SAW [7, 23, 24] resonators due to their much smaller sizes and can be batch-fabricated and utilized in highly integrated large arrays at a very low cost. However, comprehensive experimental studies on the performance and durability of such devices for particle sensing applications have not been adequately studied.

The resonators and the techniques demonstrated in this work will allow the design of low-cost handheld instruments that can determine the cumulative mass density of aerosol particles in air samples. Furthermore, through a variety of existing techniques [25–29], particles can be separated based on their size, and particles with a specific size range can be directed to different resonators in an array. In this manner, size distribution of particles can be determined. The purpose of this work is not to maximize the mass sensitivity, but rather to demonstrate suitability and robustness of thermally actuated resonators for particulate sensing applications.

2. Resonator fabrication

A single mask microfabrication process was used to fabricate the resonators on a low resistivity p-type SOI substrate with a device layer thickness of 15 μm and buried oxide layer (BOX) thickness of 5 μm . Figure 1 shows the fabrication process that starts by growing a thin (~ 200 nm) layer of thermal silicon dioxide on the substrate. The silicon dioxide layer is patterned to define the resonator structures.

The silicon structures are then carved into the SOI device layer by deep reactive ion etching (DRIE) of silicon all the

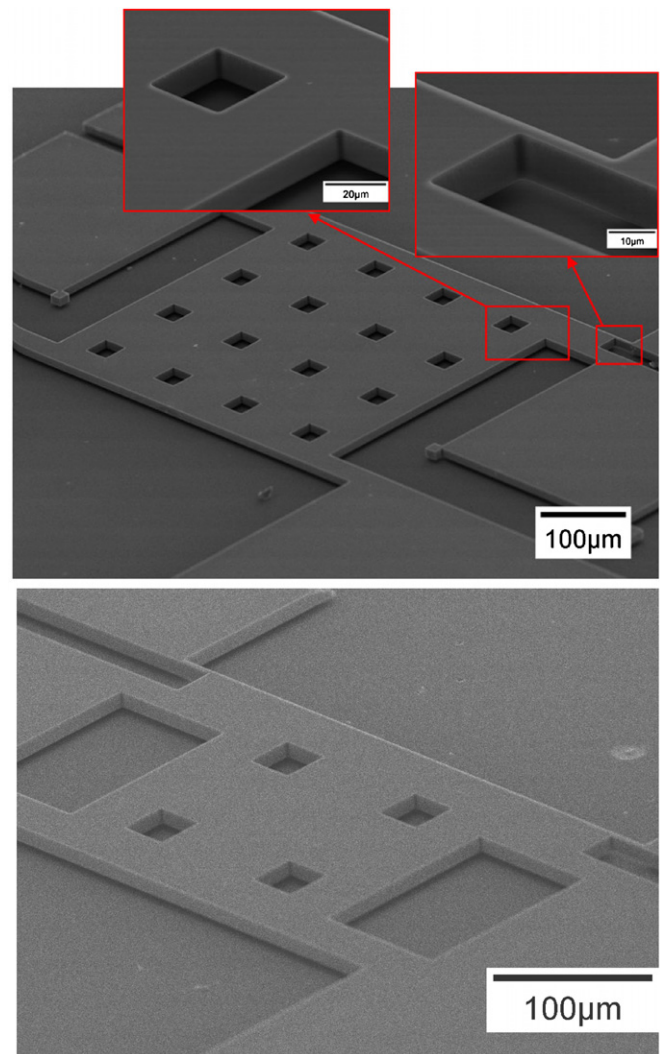


Figure 2. SEM view of two fabricated thermal-piezoresistive resonators with a sensing platform square measuring 560 and 280 μm and support length of 80 μm . The narrow actuator beam is 32 μm long and 5 μm wide.

way down to the buffer oxide layer. Finally, a 35 min dip in 49% hydrofluoric acid (HF) is performed to release the structures by etching the underlying BOX layer. At the same time the remaining oxide mask on top of the structures is also etched away. The result will be suspended single crystalline silicon resonant structures with integrated thermal actuator/piezoresistive sensors. The SEM view of two of the fabricated resonators with plate dimensions of 560 and 280 μm and support length of 85 μm are shown in figure 2.

Depending on the size of the resonating plate, a number of release holes have been etched into each plate to minimize the release time in HF and avoid excessive undercutting of the wire-bond pads.

3. Resonator characterization

Since the fabricated resonators have monolithic low resistivity silicon structures, and therefore there is no electrical isolation

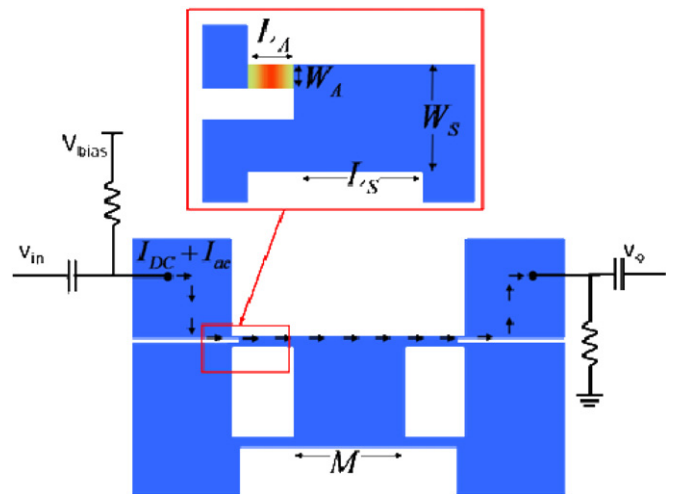
Table 1. Measured data for resonators with various dimensions and their comparison with the calculated values using the models developed in part I.

Resonator dimensions (μm)			Applied parameters		Measured parameters			Calculated parameters					
Plate size	L_A W_A	L_S W_S	I_{DC} (mA)	Vacuum/ Air	Q factor	Frequency (MHz)	g_m (mA V ⁻¹)	R_A (Ω)	Mass (μg)	C_{th} (nJ K ⁻¹)	$g_{m,calc}$ (mA V ⁻¹)	g_m/P_{DC} (F.M.)	$F.M./Q$
280	32	80	24	Vacuum	11 000	1.4144	0.621	25.6	2.77	9.09	1.10	35.7	3.245
	5	70	43	Vacuum	8200	1.4125	1.52	4.57	332 005	7.52	2.65	27.3	3.329
			55	Air	3300	1.4119	0.771				1.74	8.44	2.558
280	32	160	25	Vacuum	17 700	0.835 09	5.45	25.6	2.98	9.09	5.56	251	14.181
	5	70	50	Vacuum	13 300	0.830 52	18.0	9.14	108 303	10.1	16.8	207	15.564
			54	Air	4200	0.831 97	6.41				6.17	63.3	15.071
280	32	200	25	Vacuum	10 500	0.677 07	4.03	25.6	3.08	9.09	4.66	174	16.571
	5	70	54	Vacuum	6700	0.6696	11.9	11.4	69 171	11.8	14.0	110	16.418
			55	Air	2000	0.674 38	3.35				4.31	29.9	14.95
560	32	160	25	Vacuum	9300	0.438 39	5.66	25.6	10.5	9.09	5.86	260	27.957
	5	70	55	Vacuum	6000	0.432 74	15.9	9.14	104 821	10	18.5	151	25.167
			55	Air	3200	0.437 21	9.27				9.79	88.2	27.563
280	17	197	48	Vacuum	14 500	0.651 41	27.6	4.53	2.97	12.8	9.72	636	43.862
	15	55	60	Vacuum	14 500	0.649 72	43.3	14.3	62 813	39.6	15.2	638	44
			60	Air	4200	0.651 16	11.1				4.40	163	38.81
280	17	400	15	Vacuum	18 000	0.269	7.51	4.53	3.42	12.8	1.90	992	55.111
	15	55	48	Vacuum	13 200	0.263 96	69.5	29	10 600	118	14.5	897	67.955
			57	Air	3000	0.266 18	18.4				4.63	168	56
560	17	200	35	Vacuum	20 000	0.349 15	33.9	4.53	10.5	12.8	12.8	1451	72.55
	15	55	61	Vacuum	15 300	0.343 45	102	14.5	59 347	41.5	30.2	1444	94.379

between the two actuators embedded in each resonator, they cannot be tested in a two-port configuration. Hence, to characterize the resonators, they were tested in a one-port configuration with the two thin beams acting simultaneously as both thermal actuators and piezoresistive sensors. It should be noted that in this case the device motional current (resulting from resonance) should be extracted from the overall current passing through the resonator that includes a relatively strong resistive feed-through current on top of the resonance current. This was done by post-processing of the measured data using a MATLAB code subtracting the large feed-through signal from the measured data.

As discussed in part I, in order to generate an actuation force at the input signal frequency, a combination of dc and ac current components was applied between the two pads connected to the thermal actuators on the two sides of the structures. The silicon chip containing the resonators was placed on a printed circuit board (PCB) containing the required resistors and capacitors for ac and dc isolation. Figure 3 shows the circuit configuration used to test the resonators. Bias resistors with a value of 100 Ω and 0.1 μF isolation capacitors were used for biasing and isolation. The actuation voltage amplitude used in all measurements (v_{in}) is 1 V. Electrical connections to the resonators were provided by wedge-bonded aluminum wires.

The PCB was then placed in a vacuum chamber with electrical feed throughs. Extensive measurements were performed on several devices with different dimensions to investigate parameters of interest including resonant frequency, quality factor and motional conductance (g_m).

**Figure 3.** Schematic diagram of the electrical connections to the resonators for one-port operation and measurement.

These parameters were measured at different bias currents both under vacuum and atmospheric pressure.

Table 1 presents the measured data and their comparison with the calculated values using the equivalent electrical model developed in part I of this paper. Three different sets of data are provided for each resonator. The first row is associated with the bias current at which the highest quality factor value has been measured for the resonator under vacuum. The second row includes measurement data under vacuum with the bias current at which the highest transmission (highest motional conductance) has been measured. The third row of data has

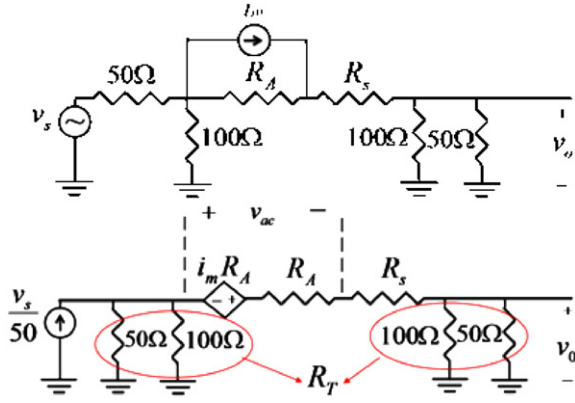


Figure 4. Electrical small-signal model used to extract the motional conductance of the resonators by de-embedding the effect of the bias resistors as well as the resistance of the resonator support beams.

been collected from the resonator operating under atmospheric pressure at its highest transmission level. Due to the very low resistance of the actuator beams of the order of a few ohms, only a small portion of the applied voltage by the network analyzer through its 50 Ω terminations will fall across the actuators resulting in excessive attenuation in the transmission spectra. Therefore, the effect of the bias resistors, the 50 Ω terminations of the network analyzer, as well as the parasitic resistances associated with the resonator structures should be de-embedded from the measured data before comparing them to the theoretically calculated values.

Figure 4 shows the electrical small signal model of the resonator along with bias resistors and the network analyzer terminations. The resonator motional conductance, which is the parameter to be extracted from the measurements, is $g_m = i_m/v_{ac}$, where v_{ac} is the ac voltage amplitude across the resonator actuators. Equation (1) gives the resonator output voltage as a function of the resonator motional current.

$$v_o = \frac{R_T \cdot R_A \cdot i_m}{2R_T + R_A + R_s}, \quad (1)$$

where R_T is the parallel combination of the 100 Ω bias resistor and the network analyzer 50 Ω impedance (i.e. 33 Ω), R_A is the resonator actuator resistance (including both actuators), and R_s is the internal parasitic resistance of the resonator which is the resistance between the two resonator pads not including the actuator resistance. R_s mainly consists of support beam resistances. Equation (1) can be rearranged as

$$i_m = \frac{v_o \cdot (2R_T + R_A + R_s)}{R_T \cdot R_A}. \quad (2)$$

On the other hand, the voltage across the resonator actuators (v_{ac}) can be calculated by dividing the thevenin-equivalent voltage of the source voltage ($v_s \cdot R_T/50$) between the series combination of $2R_T$, R_s and R_A .

$$v_{ac} = \frac{R_T \cdot R_A}{2R_T + R_A + R_s} \cdot \frac{v_s}{50}. \quad (3)$$

Combining equations (2) and (3) leads to the motional conductance of the resonator as

$$g_m = \frac{i_m}{v_{ac}} = \frac{50 \cdot (2R_T + R_A + R_s)^2}{R_T^2 \cdot R_A^2} \cdot \frac{v_o}{v_s}. \quad (4)$$

The transmission value in dB measured by the network analyzer is $T_{dB} = 20 \log \frac{2v_o}{v_s}$.

Therefore,

$$g_m = \frac{i_m}{v_{ac}} = \frac{25 \cdot (2R_T + R_A + R_s)^2}{R_T^2 \cdot R_A^2} \cdot 10^{\frac{T_{dB}}{20}}. \quad (5)$$

Motional conductance values presented in table 1 are the values after de-embedding the effect of the bias, termination and support resistances. For resonators with long and narrow ($32 \times 5 \mu\text{m}$) thermal actuator beams, most of the g_m values extracted from the measurements are in good agreement with the values predicted by the model. Considering the several possible sources of error, the discrepancies between measurement and calculation seem to be quite justified for such devices. Some of the major sources of error include errors in extraction of the measured motional conductance from the logarithmic measured transmission data (from the network analyzer) and de-embedding the parasitic resistances, uncertainty in resistivity and other physical properties of the structural material (e.g. piezoresistive coefficient) and dimensions, as well as changes in the material properties at elevated temperatures. More significant discrepancies are observed for the resonators with short and wide ($17 \times 15 \mu\text{m}$) actuators. Such errors are believed to be due to the fact that the value of the parasitic resistance (support resistance) in such devices is much larger than the resistance of the thermal actuators. Therefore, most of the applied actuation voltage is in fact applied to the support beams rather than the actuators. Considering the fact that the supports also experience significant stresses as the resonator vibrates, the effect of the supports in the resonator motional response could supersede that of the actuators.

Figure 5 shows different frequency response plots for an 830 kHz resonator at different bias currents under vacuum and atmospheric pressure. Equivalent motional conductance of as high as 18 mA V^{-1} has been extracted for this resonator, which is more than enough to be able to use such a device as an electronic component.

As expected, by increasing the dc bias current the motional current level increases while the resonator frequency decreases due to the higher static temperature and softening of the structural material. The measured resonance frequencies for resonators with different dimensions obey the expected trend, i.e. for similar support sizes, larger masses result in lower frequencies and for similar mass sizes, shorter supports result in higher flexural stiffness of the support beams, and therefore higher resonance frequencies. Furthermore, the measured figure of merit over Q values ($FM./Q$) presented in table 1 are in good agreement with the trends expected based on the analysis in part I. For example, the 0.65 and 0.34 MHz devices (fifth and seventh devices in table 1, respectively), have the same dimensions except for their central mass. As predicted in part I, the device with the larger central mass has a larger $FM./Q$. In another example, when comparing the first and second devices in table 1, which only differ in the stiffness of their support beams, the second device, which has a lower stiffness, has a larger $FM./Q$. Finally, a comparison between similar resonators with different actuator size reveals that as

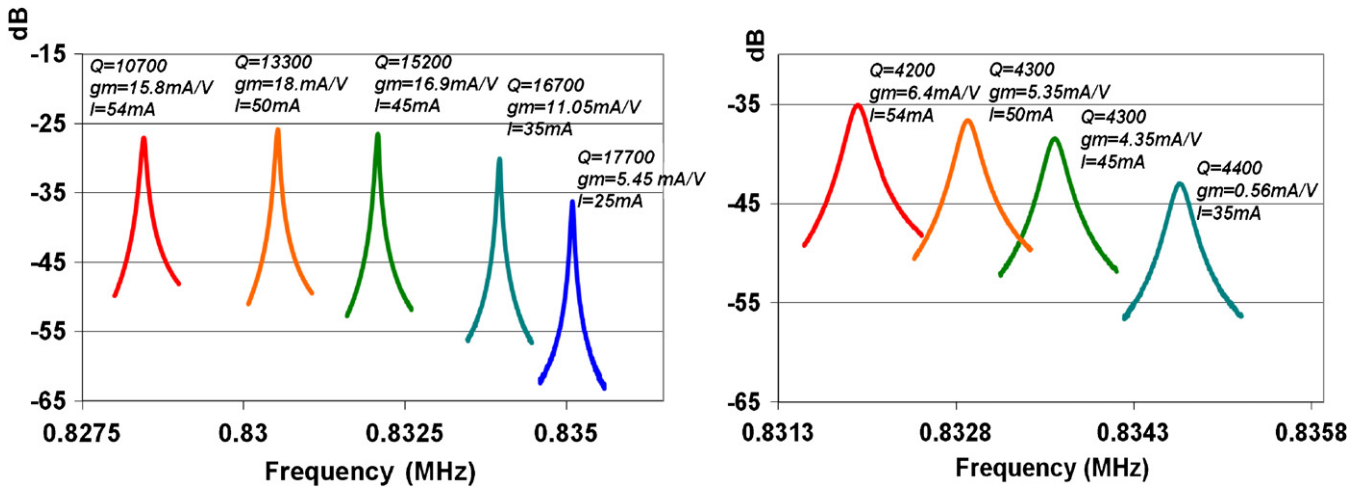


Figure 5. Measured frequency responses for a thermally actuated resonator with different bias currents. The graph on the right shows the results under vacuum while the graph on the left represents the results measured in air. The resonating device and support dimensions are 280 and 160 μm , respectively, while the actuating beam has length and width of 32 and 5 μm , respectively.

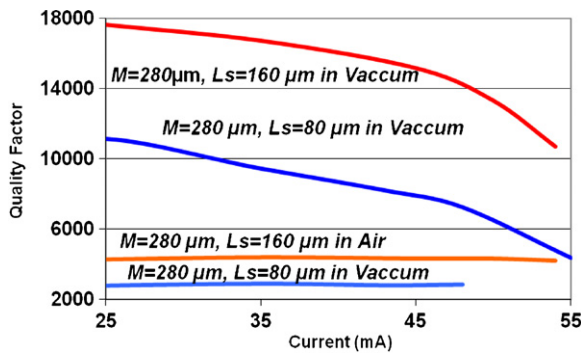


Figure 6. Measured quality factors for two thermally actuated plate resonators versus the applied bias current. The resonators have resonating mass and support lengths of 280–160 μm and 280–80 μm , respectively. Each device was tested in both vacuum and air.

expected in part I, shorter and wider actuators lead to higher $FM./Q$.

As shown in figure 6, a general trend of reduction in the quality factor is observed as the bias currents increase. Since the air viscous damping becomes the dominant loss mechanism when operating the resonators under atmospheric pressure, the effect of temperature-induced loss becomes much less pronounced.

One of the interesting and highly desirable characteristics of the resonator structures used in this work is that, as expected and discussed in part I, they maintain relatively high quality factors of the order of 2000–4500 in air. Quality factors of capacitive beam resonators with such low frequencies typically drop to 100 or less in air [19, 30–32]. This makes such resonators particularly suitable for environmental sensory applications.

4. Resonator mass sensitivity characterization

In order to measure the mass sensitivity of the fabricated resonators, aerosol particles with known size and composition

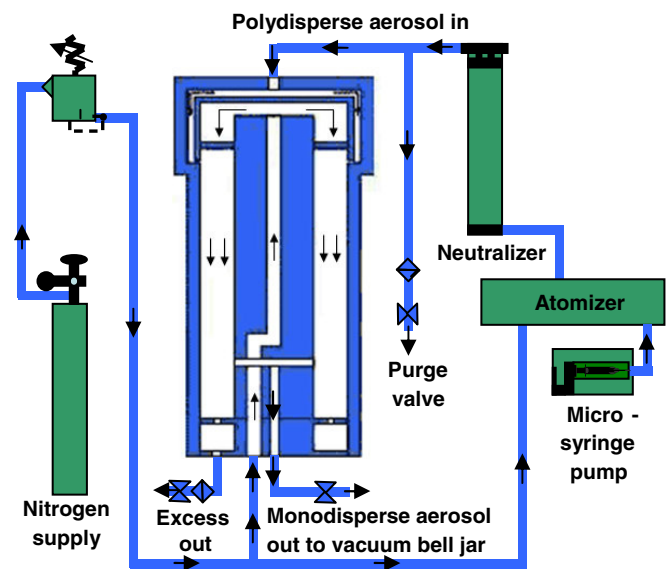


Figure 7. Schematic diagram of the aerosol particle generator. Dried aerosol is injected into the differential mobility analyzer (the central column) that permits selection of only particles with specific diameters based on its adjusted voltage and flows.

were generated and deposited on the resonators while monitoring their frequency shift. Figure 7 shows the schematic diagram of the aerosol particle generator used for this purpose. The system includes a micro syringe pump that was filled with a solution of methylene blue in ethanol. The flow of liquid coming out of the micro syringe is first turned into small droplets (atomized) by a perpendicular flow of nitrogen gas. The droplets are passed through a Kr-85 bipolar diffusion charger that neutralizes most of the charge left on the particles as a result of atomization and establishes a charge distribution close to the Boltzman distribution for the droplets (mostly neutral, some $\pm 1e$, less $\pm 2e$, etc). In the meantime, the solvent in the droplets is evaporated and the dried aerosol is injected into a differential mobility analyzer that separates the

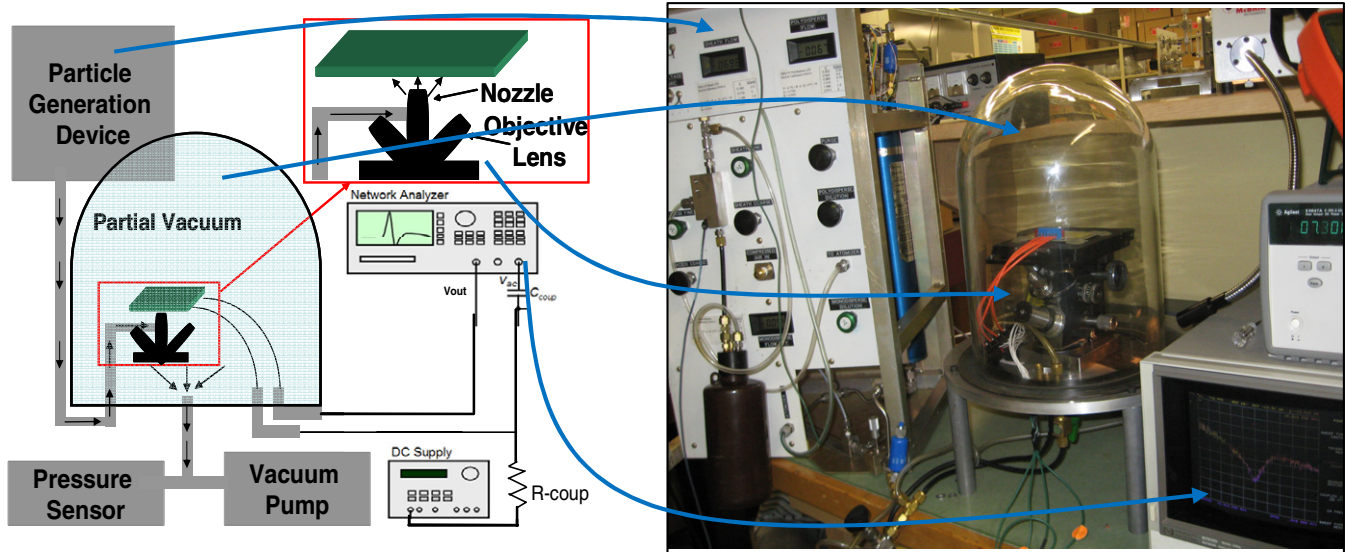


Figure 8. Aerosol particle generator and accelerator used to characterize the resonator mass sensitivities. The aerosol jet was positioned over the sensor using a modified microscope with an integrated nozzle and a micro-positioning stage.

particles using an electrostatic field (based on their mass and electric charge) allowing only particles with a specific mass to charge ratio to pass through it.

In this experiment, the voltage and flows were regulated to permit the selection of particles having a diameter near $1\ \mu\text{m}$. The particles were then directed into a low-pressure chamber comprising a bell jar, placed and sealed on a metallic plate with electrical and air feed-throughs. One of the air inlets was connected to a small vacuum pump generating a pressure of $\sim 60\text{--}80$ Torr. The flow of particles was connected to the other inlet of the chamber and the particles were deposited on the sensors through a nozzle embedded in a microscope (figure 8) with one of the objective lenses of the microscope replaced by the nozzle. The microscope is used to align the beam of particles to the resonator under test, which is mounted on a micro-positioning stage. The alignment is performed by looking at the resonator sample through the microscope and aligning the sample so that the resonator under test is in the middle of the view. The objective platform is then turned to switch to the nozzle without changing the position of the sample. As a result, the nozzle will be positioned exactly on top of the resonator under test.

Resonators with different dimensions were exposed to the flow of particles for several consecutive intervals of a few minutes each. After each interval the resonator characteristics were measured and recorded. Figure 9 shows the measured change in the resonance frequency versus the overall exposure time of a resonator with a square size of $280\ \mu\text{m}$ and support length of $400\ \mu\text{m}$, which has a frequency of $266\ \text{kHz}$. The narrow actuator beam is $17\ \mu\text{m}$ long and $15\ \mu\text{m}$ wide. It is clear that as more particles are deposited on the resonator, its resonant frequency decreases almost linearly over time.

Figure 10 shows different frequency response plots for the same resonator biased at a constant current of $30\ \text{mA}$ for an overall exposure time of $120\ \text{min}$.

It should be noted that the resonator quality factors are surprisingly robust and even after the deposition of thousands

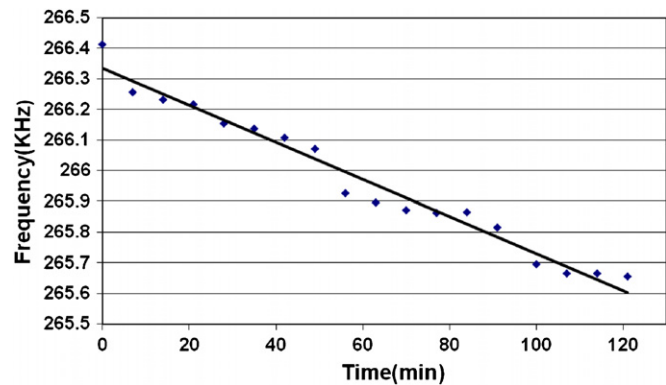


Figure 9. Change in the measured resonance frequency for a $266\ \text{kHz}$ resonator as a function of the overall exposure time showing an overall frequency shift of $\sim 760\ \text{Hz}$ (0.29%).

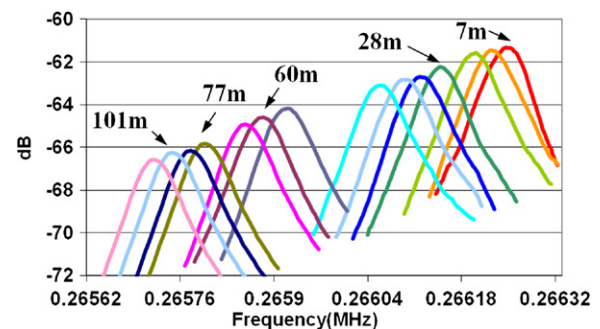


Figure 10. Measured frequency responses for the $266\ \text{kHz}$ resonator after several consecutive steps of particle deposition.

of particles, no significant Q degradation is observed. This robustness is mainly attributed to the thermal-piezoresistive nature of the resonators. An air gap capacitive resonator could not have survived such particle bombardment over such a long

Table 2. Summary of measurement results obtained from different resonators.

Resonator and support (<i>Ls/Ws</i>) Dimension (μm)	Frequency (kHz)	<i>Q</i> factor	Time (min)	Frequency shift (Hz) ^a %	ΔM from Calc. (ng)	ΔM from particle counts (ng) ~ # Particles	S_{Theory} (Hz ng ⁻¹)	S_{meas} (Hz ng ⁻¹)
280–85/55	1781.31	760	0	–475	1.45	1.7	327	280
	1781.26	870	20					
	1781.08	730	30					
	1780.83	990	45					
280–200/55	665.683	2220	0	–390	3.46	3.4	112	115
	665.458	2280	15					
	665.354	2340	30					
	665.294	2220	45					
280–400/55	266.413	3050	0	–760	19	14.9	40	51
	266.154	2890	28					
	265.926	2880	56					
	265.815	2480	91					
	265.655	2480	121					
				0.29		23 000		

^a The frequency shift values are in accordance with overall particle deposition time of 45, 45 and 121 min, respectively.

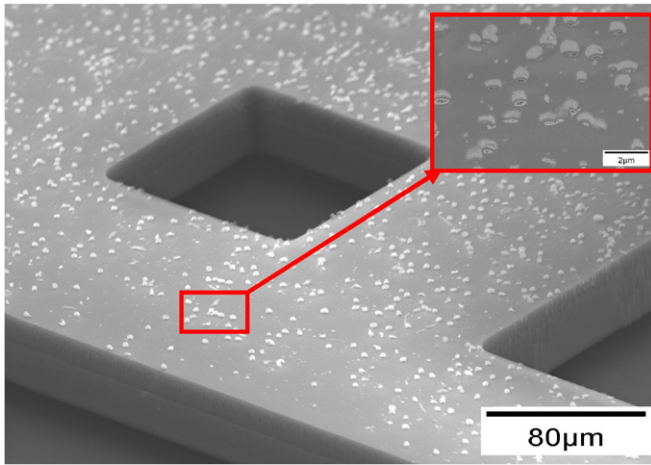


Figure 11. SEM view of part of a resonator after deposition of $\sim 1 \mu\text{m}$ diameter particles.

period as one single particle entering the transduction gaps could have completely made the resonator non-operational.

The added mass of the particles is expected to reduce the resonant frequency according to

$$f = \frac{1}{2\pi} \sqrt{\frac{k}{m}} \Rightarrow \frac{\Delta f}{f} = -\frac{\Delta m}{2m}, \quad (6)$$

where k , m and f are the stiffness, effective mass and resonant frequency of the resonator, respectively; Δf is the shift in the resonance frequency and Δm is the added particle mass.

Knowing the dimensions, and therefore the mass of the resonators, the mass of the deposited particles was estimated from the measured frequency shifts (table 2). Independently, the number of deposited particles was estimated by SEM inspections after deposition (figure 11). Partial counting and estimation methods were used to determine the approximate number of deposited particles. The overall particle mass was then calculated using

$$\Delta m = \frac{N\rho\pi d^3}{6}, \quad (7)$$

where N is the number of particles, ρ is the particle density and d is the particle diameter.

As shown in table 2, comparison of the theoretically calculated and practically estimated masses shows an acceptable agreement between the two.

Resonator mass sensitivities are in the 50–300 Hz ng⁻¹ range and as expected are higher for higher frequency devices. Orders of magnitude higher mass sensitivities can be achieved by further shrinking the size of the resonators.

Using the Allan-variance method [33], frequency measurement accuracies in the sub-0.01 Hz have been measured and reported for thermally actuated resonators with similar frequencies and quality factors in [34]. Therefore, it is expected that short-term frequency resolutions in the 0.01–0.05 Hz range should be achievable for the resonators presented here when engaged in an oscillator feedback loop. However, this limit is much smaller than the limit imposed by the temperature-induced frequency drift of the devices. Assuming a temperature uncertainty of 10 °C (which is typical in targeted environmental applications) and a temperature coefficient of frequency (TCF) of $-40 \text{ ppm } ^\circ\text{C}^{-1}$, which is typical for uncompensated silicon resonators, the frequency of a 1.7 MHz resonator could shift by up to 680 Hz due to temperature. This limits the mass resolution to $\sim 2.3 \text{ ng}$. TCF as low as $-0.05 \text{ ppm } ^\circ\text{C}^{-1}$ has been achieved for the compensated version of thermally actuated silicon resonators [35] reducing the temperature-induced frequency inaccuracy of the same 1.7 MHz resonator to 34 Hz. This translates into a mass resolution of $\sim 115 \text{ pg}$. Minimum detectable mass limits in the tens of pico-gram range [20, 36] for QCM and SAW resonators and in the pico-gram range [10, 37] for FBARs have been reported. However, such estimates generally neglect the effect of temperature-induced frequency uncertainties.

5. Airborne particle mass density measurement

After the characterization of the resonator mass sensitivities and their performance as particle mass sensors with artificially generated particles, a number of the resonators were used to

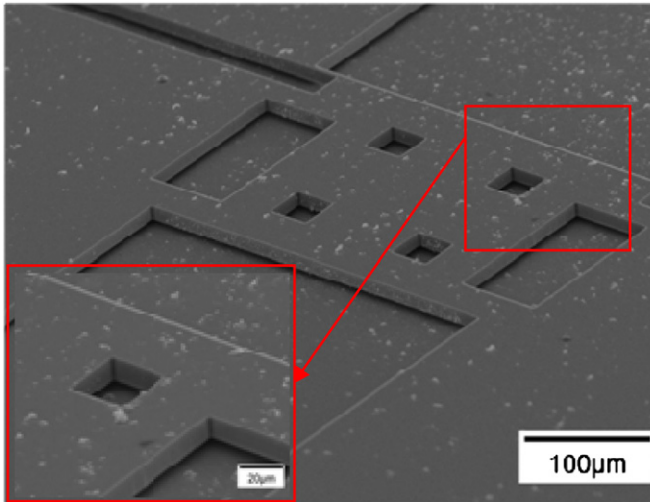


Figure 12. SEM view of the thermal resonator of figure 2 after exposure to aerosol particles in the atmosphere for 80 s.

measure the concentration of airborne particles in a regular air sample from the surrounding lab environment.

In this experiment the PCB was placed in the same low-pressure (~ 60 – 80 Torr) chamber with one of the feed-throughs connected to a small vacuum pump. The other air inlet, internally connected to the particle-deposition nozzle, was left open allowing the air from outside (along with the particles suspended in it) to be sucked into the chamber. The air and airborne particles are directed and accelerated at the narrow opening at the end of the nozzle towards the resonator. A valve was also connected to the air inlet to allow turning the particle flow on and off. With the inlet valve closed, under a constant bias current, the main parameters of interest including the resonance frequency, quality factor and resonator equivalent resistance at resonance (motional resistance) were recorded.

The inlet valve was then opened exposing the resonator under test to the air flow, and consequently the aerosol particles. The exposure was done in 10 s intervals and after each exposure the resonator parameters were measured and recorded.

A similar set of measurements were performed on different resonators with different dimensions. As expected, as a result of the added mass of the absorbed particles to the resonating body of the devices, the resonant frequency of the resonators was reduced after each exposure step. The absorbed mass (Δm) can similarly be calculated based on the measured frequency shift (Δf) and mass of the resonator itself (m) as previously shown in equation (6).

Figure 12 shows the SEM view of the resonator of figure 2(b) after it was exposed to the aerosol particles in the atmosphere for 80 s.

The calculated values for the deposited masses in each 10 s interval was in the 100–1000 pg range. Figures 13 and 14 show the change in the resonance frequency and quality factor of the resonator shown in figure 12 versus the overall exposure time.

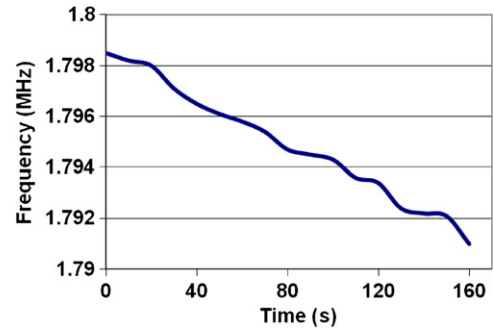


Figure 13. Change in the measured resonance frequency for the resonator shown in figure 12 as a function of the overall exposure time showing an overall frequency shift of more than 8 kHz (0.44%).

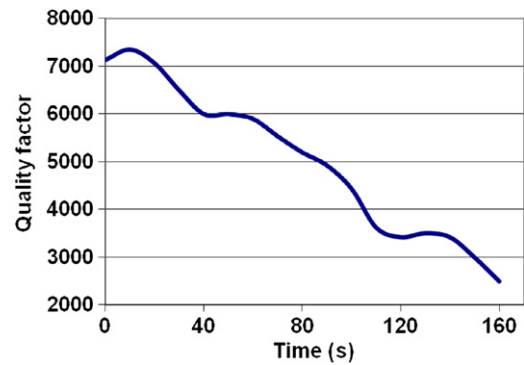


Figure 14. Measured quality factors versus overall time of exposure to aerosol particles for the resonator shown in figure 12.

To calculate the particle mass density in the air sample, equation (8) can be used to calculate the mass flow of the air entering the chamber (w) [9]:

$$w = 0.685 \frac{Ap_0}{\sqrt{RT_0}} \quad (\text{kg s}^{-1}), \quad (8)$$

where R is the ideal gas constant (287 J (kgK)^{-1}), T_0 is the temperature in kelvin, P_0 is the pressure in pascal and A is the nozzle orifice area in m^2 . Knowing the upstream air density (ρ), the upstream volumetric flow can be calculated ($F = \frac{w}{\rho}$).

By calculating F and knowing the change in mass (Δm), the aerosol mass concentration can be calculated as

$$C = \frac{\Delta m}{Ft}, \quad (9)$$

where t indicates the exposure time.

Based on the measurement results and using equations (8) and (9), a value of $14.2 \mu\text{g m}^{-3}$ was calculated for aerosol concentration in the lab environment. According to the annual environmental protection agency (EPA) report, the average PM2.5 (particles less than $2.5 \mu\text{m}$ diameter) for Denver in 2008 was $\sim 7.35 \mu\text{g m}^{-3}$ while PM10 was $\sim 25.8 \mu\text{g m}^{-3}$. The calculated value based on our experiment is in the same range, which confirms the validity of the experiment and calculations.

6. Conclusion and future work

Thermally actuated single-crystal silicon in-plane resonators with piezoresistive output detection were successfully fabricated and characterized. Frequencies in the 250 kHz to

2 MHz range and quality factors as high as 20 000 in vacuum and 4400 in air were measured for the resonators, making them ideal for sensory applications. The resonators were used for the cumulative mass measurement of airborne micro particles. Not only did the described in-plane thermally actuated flexural resonators maintain high quality factors in air, but they were also very robust and even after deposition of thousands of particles, no significant Q degradation was observed for such devices. Relatively low motional impedances in the few k Ω range obtained for the resonators is bound to make them suitable components for utilization in electronic systems. Mass sensitivities in the order of hundreds of Hz per ng were measured for such resonators, which are in good agreement with the theoretically calculated mass sensitivities. Measurement of the mass density of arbitrary airborne particles in the surrounding lab environment also shows a good agreement with the value indicated by the environmental protection agency.

Future work includes further design optimization of the resonators and shrinking their dimensions to achieve lower equivalent impedances with higher resonance frequencies, significantly lower power consumption and higher mass sensitivity allowing single-particle mass measurements. Integration of piezoresistive impact-sensing mechanisms in the sensor structures to measure the impact force of the individual particles along with their mass and characterization of such devices in more advanced aerosol collection and separation systems are among other future directions.

References

- [1] Fahey D W 2003 Twenty questions and answers about the ozone layer, in scientific assessment of ozone depletion *Proc. Global Ozone Research and Monitoring Project Report, World Meteorological Organization* vol 47 pp 182–6
- [2] Kerr J B and Seckmeyer G 2003 Surface ultraviolet radiation: past and future, in scientific assessment of ozone depletion *Proc. Global Ozone Research and Monitoring Project Report, World Meteorological Organization* vol 47 pp 134–41
- [3] Newman P A and Pyle J A 2003 Polar stratospheric ozone: past and future, in scientific assessment of ozone depletion *Proc. Global Ozone Research and Monitoring Project Report, World Meteorological Organization* vol 47 pp 156–61
- [4] Panchenko M V *et al* 2008 Active spectral nephelometry as a method for the study of submicron atmospheric aerosols *J. Remote Sens.* **29** 2567–83
- [5] Aspey R A, Brazier K J and Spencer J W 2004 Optical sensing of smoke using a polychromatic LED: combustion material identification using HLS analysis *Sens. Review* **24** 199–205
- [6] Butler J D and MacMurd S D 1976 Characterization of aerosol particulates by scanning electron microscope and X-ray energy fluorescence analysis *J. Int. Environ. Stud.* **9** 93–103
- [7] Bowers W D and Chuan R L 1991 Surface acoustic-wave piezoelectric crystal aerosol mass microbalance *Rev. Sci. Instrum.* **60** 1297–302
- [8] Stanley S M *et al* 2005 An EP-SAW for measurements of particle matter in ambient air *J. Nondestruct. Test. Eval.* **20** 3–7
- [9] Baron P A and Willeke K 2001 *Aerosol Measurement, Principles, Techniques and Applications* 2nd edn (New York: Wiley-Interscience)
- [10] Black J P 2007 MEMS-enabled miniaturized particulate matter monitor employing 1.6 GHz aluminum nitride thin-film bulk acoustic wave resonator (FBAR) and thermophoretic precipitator *Proc. IEEE Ultrasonics Symp.* pp 476–80
- [11] Hajjam A *et al* 2009 Thermally actuated MEMS resonant sensors for mass measurement of micro/nanoscale aerosol particles *Proc. IEEE Sensors* pp 707–10
- [12] Hajjam A 2010 Fabrication and characterization of resonant aerosol particle mass sensors *Proc. IEEE MEMS* pp 863–6
- [13] Kim J H *et al* 2009 High sensitivity capacitive humidity sensor with a novel polyimide design fabricated by MEMS technology *Proc. 4th Int. IEEE Conf. Nano/micro Engineered and Molecular Systems (China, January 2009)* pp 703–6
- [14] Ekinci K L, Yang Y T and Roukes M L 2004 Ultimate limits to inertial mass sensing based upon nanoelectromechanical systems *J. Appl. Phys.* **95** 2682–9
- [15] Lavrik N V and Datskos P G 2003 Femtogram mass detection using photothermally actuated nanomechanical resonators *Appl. Phys. Lett.* **82** 2697–9
- [16] Yang Y T *et al* 2006 Zeptogram-scale nanomechanical mass sensing *Nano Lett.* **6** 583–6
- [17] Burg T P and Manalis S R 2003 Suspended microchannel resonators for biomolecular detection *Appl. Phys. Lett.* **83** 2698–700
- [18] Li C and Chou T 2004 Mass detection using carbon nanotube-based nanomechanical resonators *Appl. Phys. Lett.* **84** 5246–8
- [19] Arcamone *et al* 2006 Micro/nanomechanical resonators for distributed mass sensing with capacitive detection *J. Microelectron. Eng.* **83** 1216–20
- [20] Rodriguez-Pardo L *et al* 2005 Sensitivity, noise and resolution in QCM sensors in liquid media *J. IEEE Sens.* **5** 1251–8
- [21] Woods D C and Chuan R L 1979 Aerosol characterization with a quartz crystal microbalance cascade impactor *Proc. Adv. Particulate Sampling Meas.* **22** 1639–45
- [22] Leskinen J *et al* 2009 Diffusion-based nanoparticle monitor using QCM technology *Proc. European Aerosol Conf.* pp 247–50
- [23] Bhide T M *et al* 2001 Shear horizontal surface acoustic wave Sensor platform development for chemical and biological detection *J. Anal. Chem.* **73** 5937–44
- [24] Berkenpas E *et al* 2004 Pure shear horizontal SAW biosensor on langasite *IEEE Trans. Ultrason. Ferroelectr. Freq. Control* **51** 1404–11
- [25] Allan J D *et al* 2003 Quantitative sampling using an aerodyne aerosol mass spectrometer: 1. Techniques of data interpretation and error analysis *J. Geophys. Res.* **108** 4090
- [26] Huang L R *et al* 2004 Continuous particle separation through deterministic lateral displacement *J. Sci.* **304** 987–90
- [27] Hitchings A, O'Doherty T and Syred N 1997 Submicrometre particle separation via high-speed gas centrifuges *J. Process. Mech. Eng.* **211** 17–29
- [28] Kim Y H *et al* 2007 Micromachined cascade virtual impactor with a flow rate distributor for wide range airborne particle classification *Appl. Phys. Lett.* **91** 043512
- [29] Liang D *et al* 2010 A miniature system for separating aerosol particles and measuring mass concentrations *J. Sensors* **10** 3641–54
- [30] Rahafrooz A *et al* 2009 Detection of sub-ppm traces of aqueous heavy-metal ions using micro-electro-mechanical beam resonators *J. Micromech. Microeng.* **19** 115003
- [31] Yi Y, Rahafrooz A and Pourkamali S 2009 Analysis of the collective effects of thermoelastic and fluid damping on silicon beam resonators *J. Micro/Nanolithography, MEMS, and MOEMS (JM3)* **8** 023010/1–7
- [32] Ahn Y, Guckel H and Zook J D 2001 Capacitive microbeam resonator design *J. Micromech. Microeng.* **11** 70–80

- [33] Allen D W and Barnes J A 1981 A modified Allan variance with increased oscillator characterization ability *Proc. Freq. Control Symp.* 470–5
- [34] Seo J H and Brand O 2008 High Q -factor in-plane-mode resonant microsensor platform for gaseous/liquid environment *J. Microelectromech. Syst.* **17** 483–93
- [35] Hajjam A, Rahafrooz A and Pourkamali 2010 Sub-100 ppb/ $^{\circ}\text{C}$ temperature stability in thermally actuated high-frequency silicon resonators via degenerate phosphorous doping and bias current optimization crystal oscillators *Proc. International Electron Device Meeting (IEDM)* at press (to appear in proceedings)
- [36] Ward M and Buttry D 1989 *In situ* interfacial mass detection with piezoelectric transducers *J. Sci.* **249** 1000–6
- [37] Weber J *et al* 2006 Shear mode FBARs as highly sensitive liquid biosensors *J. Sensors Actuators* **128** 84–8